Correspondence to:
E. N. Curchitser,
enrique@marine.rutgers.edu

Interannual Variability of the Mid-Atlantic Bight Cold Pool

Zhuomin Chen[1,2] (iD) and Enrique N. Curchitser[3] (iD)

[1]Department of Marine and Coastal Sciences, Rutgers University, New Brunswick, NJ, USA, [2]Now at Woods Hole Oceanographic Institution, Woods Hole, MA, USA, [3]Department of Environmental Sciences, Rutgers University, New Brunswick, NJ, USA

Abstract The Mid-Atlantic Bight (MAB) Cold Pool is a bottom-trapped, cold (temperature below 10°C) and fresh (practical salinity below 34) water mass that is isolated from the surface by the seasonal thermocline and is located over the midshelf and outer shelf of the MAB. The interannual variability of the Cold Pool with regard to its persistence time, volume, temperature, and seasonal along-shelf propagation is investigated based on a long-term (1958–2007) high-resolution regional model of the northwest Atlantic Ocean. A Cold Pool Index is defined and computed in order to quantify the strength of the Cold Pool on the interannual timescale. Anomalous strong, weak, and normal years are categorized and compared based on the Cold Pool Index. A detailed quantitative study of the volume-averaged heat budget of the Cold Pool region (CPR) has been examined on the interannual timescale. Results suggest that the initial temperature and abnormal warming/cooling due to advection are the primary drivers in the interannual variability of the near-bottom CPR temperature anomaly during stratified seasons. The long persistence of temperature anomalies from winter to summer in the CPR also suggests a potential for seasonal predictability.

Plain Language Summary The interannual variability of the Mid-Atlantic Bight (MAB) Cold Pool is investigated based on a long-term (1958–2007) high-resolution regional numerical model of the northwest Atlantic Ocean. The Cold Pool is a relatively cold and fresh water mass that exists below the surface and is located over the mid-shelf and outer-shelf of MAB. A Cold Pool Index (CPI) is defined and computed based on its persistence time, volume, temperature, and seasonal along-shelf propagation and is used to quantify the strength of the Cold Pool in different years. The Cold Pool years are then categorized as strong, weak, and normal years based on the CPI. A detailed quantitative heat budget study of the Cold Pool region (CPR) has been examined in order to expose the main drivers of the interannual variability. Results suggest that the initial winter-time temperature and warming/cooling due to advection are the primary drivers in controlling the interannual variability of the near-bottom CPR temperature during spring and summer. The long persistence of temperature anomalies from winter to summer in the CPR also suggests a potential for seasonal predictability of the Cold Pool.

1. Introduction

The Mid-Atlantic Bight (MAB) is one of the most ecologically and economically important habitats of the northeast United States continental shelf. Over the past few decades, the MAB shelf warming has been documented not only in the surface layer (Friedland & Hare, 2007; Fulweiler et al., 2015; Shearman & Lentz, 2010) but also in near-bottom waters (Forsyth et al., 2015; Kavanaugh et al., 2017). Ocean warming has been associated with declines of abundances and poleward shifts of distribution of cold-water species over the northeast United States continental shelf (Gawarkiewicz et al., 2014; Nye et al., 2009, 2011). As a seasonally prominent thermal feature, the Cold Pool exerts a strong influence on the recruitment and settlement of several cold-temperature fish species in the MAB ecosystem (Miller et al., 2016; Sullivan et al., 2005) as well as phytoplankton and zooplankton productivity (Bi et al., 2014; Flagg et al., 1994).

The Cold Pool is a bottom-trapped cold and fresh (temperature usually below 10°C and practical salinity below 34) water mass isolated from the surface by a seasonal thermocline, located over the midshelf and outer shelf of the MAB. The spatial and seasonal variability of the Cold Pool has been investigated by using both observations and models (Chen et al., 2018; Houghton et al., 1982; Lentz, 2017). It is a continuous and nonstationary feature that experiences an annual cycle of *onset-peak-decline*. It first emerges around early
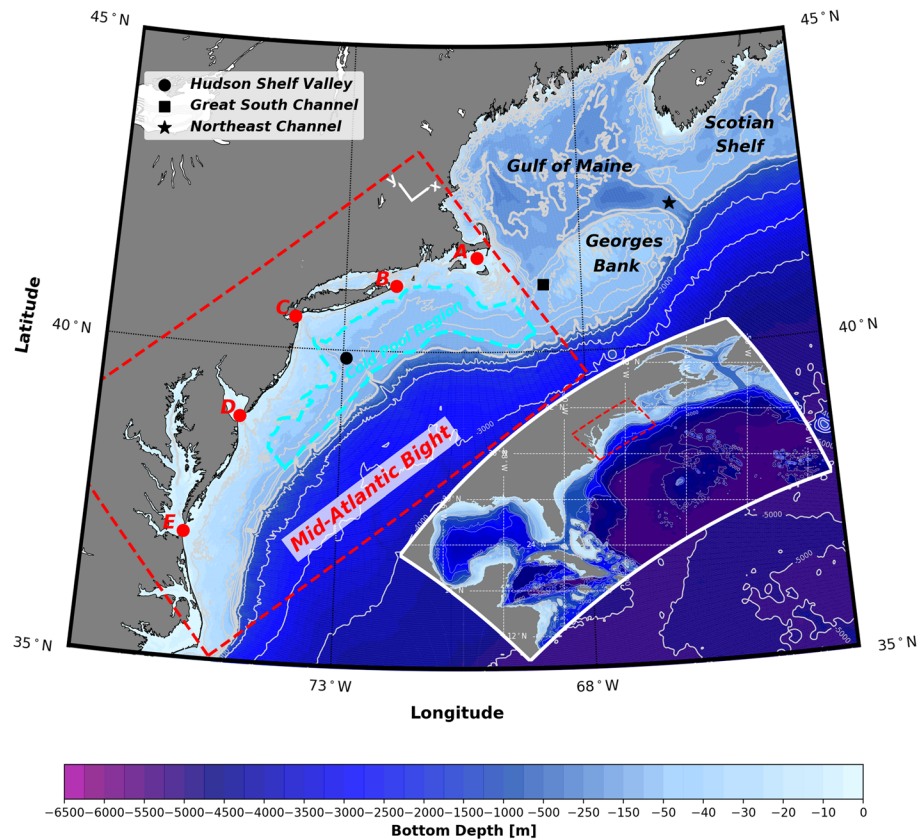
Figure 1. Bathymetry of the study area—the MAB continental shelf (located within the red dashed box in the background) and the ROMS model domain (lower right white box). Depth contours of both the study area and model domain are given at 0, 20, 40, 60, 80, 100, 200, 1,000, 2000, 3,000, 4,000, and 5,000 m (light gray lines), among which the 200-m isobaths are thickened. Special topography, such as the HSV, the Great South Channel, and the Northeast Channel, are marked with different markers (shown in the upper left corner). Five along-shelf geographical locations are marked as follows: A—Nantucket Shoals, B—Montauk Point, C—Sandy Hook, D—Delaware Bay, and E—Chesapeake Bay. The cyan dashed line over the MAB continental shelf suggests the horizontal extent of the CPR (between 40- and 100-m isobaths, from location A to D), which is the control volume for the heat budget analysis in section 4. The along-shelf (x) and across-shelf (y) directions of the model grid are shown in the upper right corner of the dashed red box of the MAB.

April, reaches its maximum volume around mid-May, and then gradually disappears around mid-September. The core of the Cold Pool (where the minimum temperature of the water mass is located) has been recorded to travel along the 60-m isobath at a speed of 2–3 cm/s on a 50-year average, from south of the New England shelf (NES) to the Hudson Shelf Valley (HSV) (Chen et al., 2018).

Differing theories were proposed regarding the origins of the Cold Pool. Fundamentally, there are two possible sources of the Cold Pool, which can be classified as having local or remote origins. The remnant winter water over the MAB continental shelf is considered the local source. Past work suggests that the Cold Pool forms with strong winter mixing and becomes isolated from the surface due to the onset of summer stratification in the water column, with no renewal from upstream sources (Bigelow, 1933; Houghton et al., 1982; Ketchum & Corwin, 1964; Ou & Houghton, 1982). The upstream cold water sources, such as cold waters from the Gulf of Maine and Georges Bank (GB), are considered as remote source of the Cold Pool (Brown et al., 2015; Fairbanks, 1982; Han & Niedrauer, 1981; Hopkins & Garfield, 1979). Based on a lead-lag correlation analysis on the near-bottom temperature anomalies of the MAB and GB, Chen et al. (2018) suggests that the Cold Pool not only originates from winter remnant water over Nantucket Shoals but also has an upstream source traveling from the southern flank of GB along the 80-m isobath during the spring.
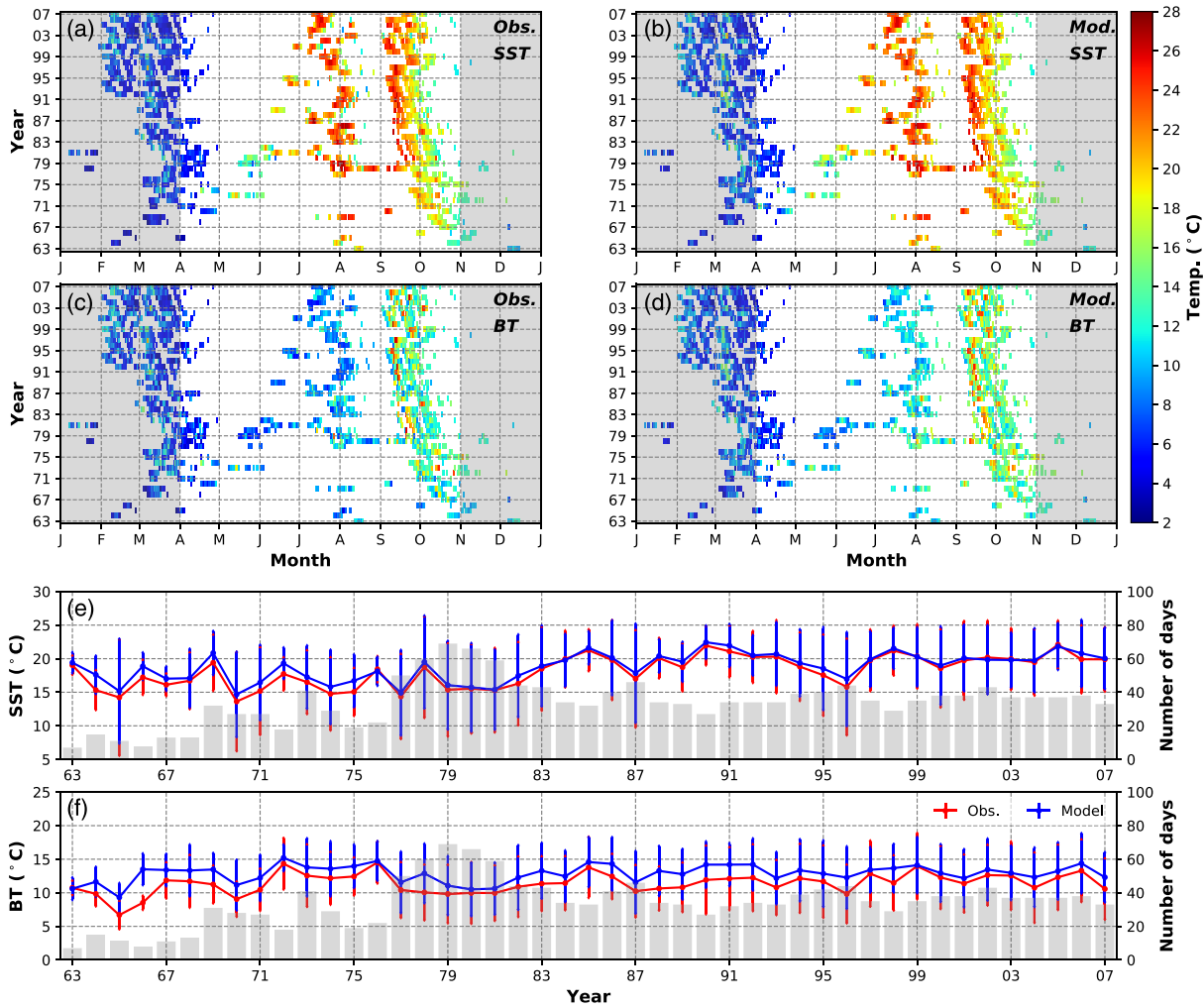
Figure 2. Model evaluation with SST and BT from the bottom trawl survey data sets on interannual timescale. (a and b) Comparison of observed SST (a) and model SST (b) over the MAB continental shelf from 1963 to 2007, with *x* axis representing days within a year from January to December and *y* axis representing years from 1963 to 2007. (c and d) Same as (a) and (b) except for (c) observed BT and (d) model BT. (e and f) Comparison of yearly binned (e) SST and (f) BT time series during stratified months (April–October) between observation (red) and model (blue). The gray bars in the background represent number of observational days within each year. Error bars of each line represent plus/minus one standard deviation (STD) of each variable.

Due to limited observations over long periods, the interannual characteristics and long-term variability of the Cold Pool are still widely unknown. In this study, we investigate the interannual variability based on a 50-year (1958–2007) high-resolution model of the northwest Atlantic (NWA) Ocean (Kang & Curchitser, 2013, 2015). Strong and weak Cold Pool years are categorized and compared according to a derived Cold Pool Index (CPI), which quantifies the strength of the specific event on the interannual timescale. We further investigate the dominant factors impacting the interannual variability of the Cold Pool temperature by carrying out an analysis of the heat balance in the Cold Pool region (CPR) based on the numerical model.

This paper is organized as follows: In section 2, we introduce the high-resolution model, model evaluation on the interannual timescale, and the Cold Pool quantification methods. In section 3 we present the interannual variability of the Cold Pool characteristics and the summer evolution during the categorized strong and weak Cold Pool years. In section 4, we present the heat budget of the near-bottom CPR, and the relative importance of ocean advection and vertical diffusion is investigated with an emphasis on strong and weak Cold Pool years. Finally, in section 5 we discuss and summarize the results.

2. Methods

2.1. Model and Cold Pool Quantification

The long-term (1958–2007) high-resolution (~7 km in the horizontal; 40 vertical terrain-following levels) numerical simulation of the NWA Ocean was performed with the Regional Ocean Modeling System (ROMS), a split-explicit, free-surface, terrain-following, hydrostatic, primitive equation (Shchepetkin & McWilliams, 2005). The model grid and the model settings that include vertical mixing scheme, initial and oceanic boundary conditions, atmospheric forcing, river discharges runoff, and tides have been described in detail in previous studies (e.g., Chen et al., 2018; Kang & Curchitser, 2013, 2015). Model standard circulation state variables are archived at a daily interval. The study domain covers the MAB continental shelf (depth<200 m), between the Cape Hatteras and Cape Cod (Figure 1).

We followed the same quantification method to capture the Cold Pool characteristics in the ROMS model as described in detail in Chen et al. (2018). This method is implemented following the historical definition of the Cold Pool, which identifies waters with specific temperature (below 10°C), salinity (practical salinity below 34), stratification (when stratification occurs), and location (below the mixed-layer depth and between 20- and 200-m isobaths over the MAB continental shelf) criteria. The climatology of the Cold Pool and its seasonal properties based on a 50-year average was investigated in Chen et al. (2018) during its onset-peak-decline cycle. In this study, we focus on the interannual variability of the Cold Pool based on the same quantification method and explore the time series of the Cold Pool characteristics (persistence, volume, temperature, etc.) from 1958 to 2007.

2.2. Model Evaluation on the Interannual Timescale

Extensive model evaluation against observations in Chen et al. (2018) shows that the model is capable of simulating the spatiotemporal variability of the shelf temperature on seasonal timescales. For this study, two long-term observational data sets have been used to further validate the model skill on interannual timescales: (1) the sea surface temperature (SST) and bottom temperature (BT) over the MAB from the bottom trawl survey data sets, calibrated by the Northeast Fisheries Science Center (1963–2007; http://comet.nefsc.noaa.gov/cgi-bin/ioos/ioos.pl) and (2) the monthly observational SST and BT gridded (0.2° × 0.2°) data sets between 1950 and 2010 over the MAB continental shelf from Richaud et al. (2016). We use the inverse distance weighting method for model interpolation (Chen et al., 2018) followed by spatial averaging for the MAB region and time averaging for each year to evaluate against the observed sea surface and bottom temperatures. We follow a similar approach to evaluate with the gridded observational data set. For both comparisons, we focus only on the stratified seasons during each year—approximately from the start of April to the end of October.

Model comparison with the bottom trawl survey data set suggests that the model is capable of capturing not only the seasonal signature but also the interannual variability in both SST and BT on the MAB continental shelf (Figure 2). The model consistency in representing the cooler BT relative to SST during stratified seasons suggests that the model is capable of resolving the vertical thermal structure throughout all 50 years of simulation that is also seen in the observations (Figures 2a–2d). We note that the model is systematically warm biased in the BT during the stratified seasons (Figures 2c and 2d). Comparison of the yearly binned SST and BT time series over the stratified seasons suggests that the model has an average warm bias of 0.62 ± 0.84°C in SST and 1.48 ± 1.72°C in BT (Figures 2e and 2f). The model successfully captures the interannual variability of both SST and BT during stratified seasons (April–October), with correlation coefficients of about 0.97 for SST and 0.82 for BT (both $p < 0.01$; Figures 2e and 2f). The warm biases in SST and BT are consistent over the time series, and values are within the root-mean-square error.

We also compared model SST and BT against the long-term (1950–2010) monthly gridded observational SST and BT data sets (Richaud et al., 2016) over the MAB continental shelf on the interannual timescale (Figure 3). Results suggest that the model hindcast compares very well with the observations, though the model is similarly warm biased by about 0.93 ± 1.08°C and 1.54 ± 1.63°C on average in SST and BT during the stratified seasons, respectively. Consistently, both the SST and BT time series are highly correlated, which suggests that the model is a credible tool for investigating the thermal feature of the Cold Pool over the MAB continental shelf.
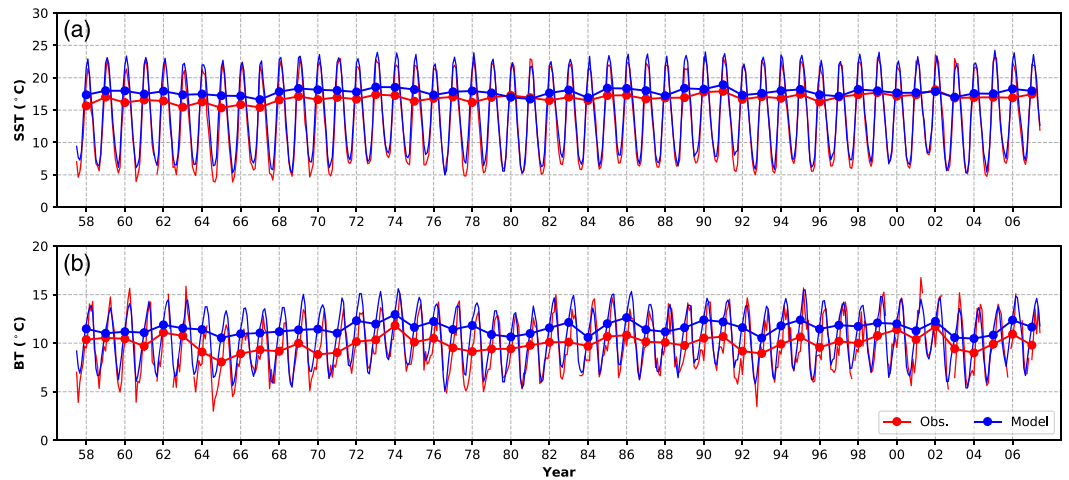
Figure 3. Model comparison with the long-term (1958–2007) gridded observational SST and BT from Richaud et al. (2016). (a) Monthly time series of the modeled (blue) and observational (red) SST, represented by thin solid lines. Yearly time series of the modeled (blue) and observational (red) SST during the stratified seasons (April–October), represented by the dotted lines. (b) Same as (a) but for BT.

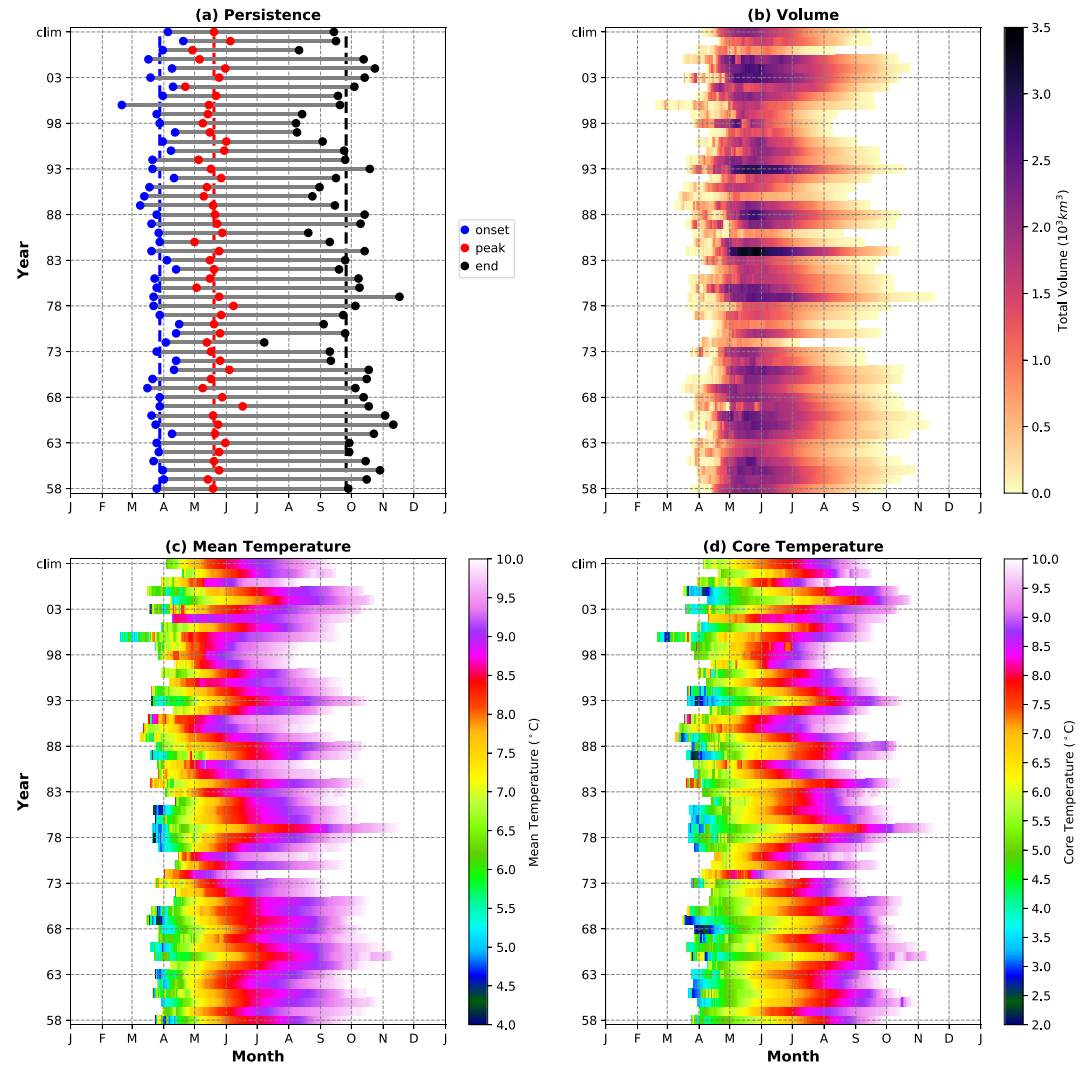## 3. Interannual Variability of the Cold Pool

In this section, we examine the interannual variability of the MAB Cold Pool with respect to its persistence, volume, temperature, and warming rates based on the Cold Pool quantification method. The Cold Pool strength is evaluated by defining and computing a CPI. We, then, investigate Cold Pool characteristics during strong and weak Cold Pool years.

3.1. Persistence, Volume, and Temperature of the Cold Pool

The Cold Pool typically experiences an onset-peak-decline cycle during its annual lifespan (Chen et al., 2018). However, the timing of the Cold Pool lifecycle varies from year to year (Figure 4a). On average, the duration of the Cold Pool during the 50 years (1958–2007) is 182 ± 30 days (about 6 ± 1 months). The onset of the Cold Pool happens on Calendar Day (CD) 87 ± 11 (end of March), on average, ranging from CD 50 (mid-February; year 2000) to CD 110 (end of April; year 2007). The average peak day is on CD 140 ± 10 (mid-May), ranging from CD 112 (end of April; year 2002) to CD 168 (mid-June; year 1967). The average end day is on CD 269 ± 26 (end of September), which has the largest interannual variation, ranging from CD 189 (early July; year 1974) to CD 321 (mid-November; year 1979). Therefore, the annual duration of the Cold Pool is strongly dependent on the end of the decline of the Cold Pool.

The Cold Pool volume also exhibits pronounced interannual variability (Figure 4b). For the years 1984 and 1993, the peak of the Cold Pool volume reaches above 3.0×10^3 km^3, while for the years 1974 and 1986, the peak volume is less than one third ($<1.0 \times 10^3$ km^3). Similarly, the annual time-integrated Cold Pool volume for each year suggests larger variations, ranging from about 0.47×10^5 km^3 of year 1974 to about 3.25×10^5 km^3 of year 1984. For clarity, these extreme values and comparison with the 50-year averages are summarized in Table 1. Results from cross-correlation analysis indicates that the annual time-integrated volume is highly correlated with the peak Cold Pool volume ($r = 0.92$; $p < 0.05$; Figure 5a) and with the larger the peak volume, the longer the persistence of the Cold Pool ($r = 0.64$; $p < 0.05$).

The volume-averaged Cold Pool temperature increases by 0.78°C/month (averaged over the 50 years) over the annual cycle, starting at about 5.5°C. However, the Cold Pool initial temperatures and warming rates during the 50 years also indicate strong interannual variability (Figure 4c). The average initial temperatures of the years 1963, 1978, and 1980 are only around 4°C, while it could reach as high as about 8.5°C as seen in 2002 (Table 1) and above 7°C for the years 1972, 1974, and 1976. Similarly, the annual average temperature of the Cold Pool exhibits high coherency with the average initial temperature ($r = 0.81$; $p < 0.05$; Figure 5b). Cross-correlation results suggest that the Cold Pool average initial and annual mean temperature are both negatively correlated with persistence time (both $r = -0.62$; $p < 0.05$), which suggests that the lower the

Figure 4. Interannual variations of the Cold Pool with respective to its persistence, volume, mean temperature, and Cold Pool core temperature from 1958 to 2007. (a) Onset (blue dots), peak (red dots), and end (black dots) time in CD of the Cold Pool for all 50 years, with x axis representing days within a year and y axis representing years from 1958 to 2007, followed by the climatology of all 50 years. The dashed vertical lines in three different colors represent the average onset (blue; CD 87), peak (red; CD 140), and end (black; CD 269) time of all 50 years. (b) Seasonal and interannual variation of the Cold Pool total volume (10^3 km^3) in daily timescale from 1958 to 2007. The x and y axis are exactly the same in (a). (c and d) Same as (b) but for the Cold Pool volume-averaged temperature and core temperature (°C).

initial/annual mean temperature of the Cold Pool, the longer the persistence. In addition, they are also negatively correlated with the annual time-integrated Cold Pool volume ($r = -0.41$ and -0.60, respectively; both $p < 0.05$) and the peak volume ($r = -0.34$ and -0.49, respectively; both $p < 0.05$).

In a similar manner, the Cold Pool core temperature (minimum temperature of the water mass) has coherent interannual variability with its volume-averaged temperature ($r = 0.92$; $p < 0.05$; Figure 4d), except that the annual average increasing trend of the core temperature is about 1.10°C/month (average of the 50 years), starting at 3.82°C, on average. Likewise, the initial core temperature is around 2°C in years 1968, 1987, 1993, and 2005 but could reach as high as 6.5°C in 2002 and around 5.6–6.0°C in years 1974, 1975, and 1976. As expected, the initial and annual average of the Cold Pool core temperatures are both negatively correlated with the persistence ($r = -0.68$ and -0.66, respectively; both $p < 0.05$). Cross-correlation analysis also suggests that the annual average core temperature is negatively correlated with the annual time-integrated and peak Cold Pool volume ($r = -0.61$ and -0.58, respectively; $p < 0.05$), the same as the initial core temperature ($r = -0.54$ and -0.48, respectively; $p < 0.05$).

Table 1
Persistence, Volume, Temperature, and Warming Rates of the Cold Pool Events During 1958–2007 for the 50-Year Average and the Extreme Years

Persistence	50-year average	Minimum/earliest	Maximum/latest
Duration	182 ± 30 days	97 days (1974)	241 days (1979)
Onset	CD 87 ± 11	CD 50 (2000)	CD 110 (2007)
Peak	CD 140 ± 10	CD 112 (2002)	CD 168 (1967)
End	CD 269 ± 26	CD 189 (1974)	CD 321 (1979)
Volume	50-year average	Minimum volume	Maximum volume
Peak	$2.11 \pm 0.54 \times 10^3$ km^3	0.87×10^3 km^3 (1986)	3.49×10^3 km^3 (1984)
Total	$1.73 \pm 0.64 \times 10^5$ km^3	0.47×10^5 km^3 (1974)	3.25×10^5 km^3 (1984)
Temperature	50-year average	Minimum temperature	Maximum temperature
Initial	5.56 ± 1.00°C	3.65°C (1980)	8.53°C (2002)
Annual-mean	8.51 ± 0.32°C	7.96°C (1969)	9.24°C (1976)
Core	3.79 ± 1.06°C	1.93°C (1968)	6.52°C (2002)
Warming rates	50-year average	Minimum rates	Maximum rates
Annual-mean	0.78 ± 0.14°C/month	0.26°C/month (2002)	1.04°C/month (1999)
Core	1.10 ± 0.16°C/month	0.60°C/month (2002)	1.47°C/month (2006)

3.2. Cold Pool Warming Rates

Initial temperature and warming rate are two important factors impacting the Cold Pool temperature on the interannual timescale as well as the volume and persistence. The average warming rate of the whole water mass (0.78°C/month) is slightly slower than the Cold Pool core warming rate (1.10°C/month), on average (Table 1); however, they are coherent with each other over the 50-year time record ($r = 0.61$; $p < 0.05$). The average warming rate of the whole cold water mass ranges from 0.56°C/month in 1995 to 1.04°C/month in 1999 and 1.01°C/month in 2006, except for year 2002, when the warming rate is only about 0.26°C/month (Figure 5d). Year 2002 is an unusual year for which the rule does not apply ("the colder/warmer initial temperature, the longer/shorter persistence"). In 2002, although both the initial temperature and initial core temperature are considerably higher than other years, the persistence (177 days), peak volume (2.2×10^3 km^3), and annual time-integrated volume (2.1×10^5 km^3) of the Cold Pool remain similar to the average values of all 50 years, which is probably due to its extremely slow warming rate.

Analysis of the core warming rate indicates that the Cold Pool core warms at a rate (0.60°C/month) in 2002. During other years, the core warming rate ranges from 0.85°C/month in 1966 to 1.46°C/month in 1997 and 1.47°C/month in 2006 (Figure 5d). Cross-correlation analysis suggests that the core warming rate is negatively correlated with the persistence ($r = -0.45$; $p < 0.05$), but less correlated with the time integrated and peak volume ($r = -0.38$ and -0.26, respectively; $p > 0.05$). The average warming rate of the whole water mass does not have significant correlations.

3.3. Cold Pool Strength

In order to investigate the strength of the Cold Pool events on the interannual timescale, we construct a CPI (Figure 5e) based on the Cold Pool's persistence time, volume magnitude, and volume-averaged temperature. We define the CPI as the time integral of the Cold Pool volume (V) multiplied by the difference between the Cold Pool temperature (T) and the threshold temperature value (T_t) during each year and then normalized by subtracting its 50-year mean and dividing by the STD:

$$\text{CPI} = <\int V \cdot (T_t - T)\, dt > ; \ T_t = 10°C, \tag{1}$$

where V and T represent the Cold Pool total volume and volume-averaged temperature during each year and T_t is the threshold value (10°C) for the temperature criterion (Chen et al., 2018). The symbol <> represents the standardization operation, which could be expressed as $<x> = (x - \bar{x})/\sigma$, where $\bar{x}$ is the mean and σ is the STD.
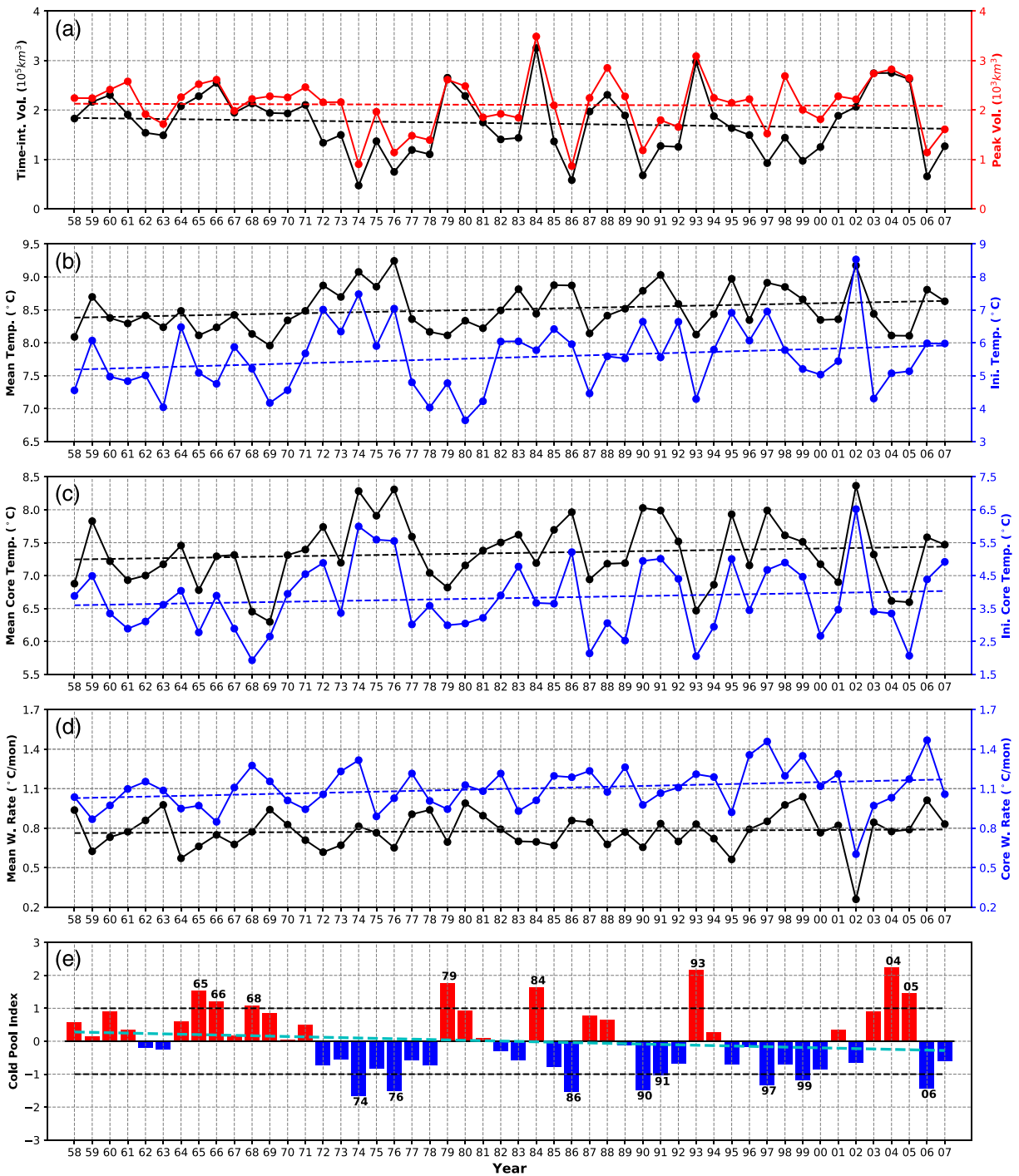
Figure 5. Time series of the Cold Pool annual time-integrated and peak volume, annual mean, and initial volume-averaged temperature and core temperature, mean and core warming rates, and the CPI from 1958 to 2007. (a) The annual time-integrated (black; 10^5 km^3) and peak (red; 10^3 km^3) Cold Pool volume with their linear trends (dashed lines). (b and c) Same as (a) but for (b) the annual mean (black) and initial (blue) volume-averaged Cold Pool temperature and (c) its core temperature with their linear trends over the time period. (d) The time series of average Cold Pool warming rates (black; °C/month) and its core warming rates (blue; °C/month) of the Cold Pool. Dashed lines represent their linear trends. (e) The CPI time series and its linear trends (cyan dashed line). The positive values of CPI (red bars) indicate strong Cold Pool events, and negative CPIs (blue bars) indicate weak events. The black horizontal dashed lines represent one STD of the CPI time series. Strong (weak) Cold Pool years are labeled for those above (below) one STD.
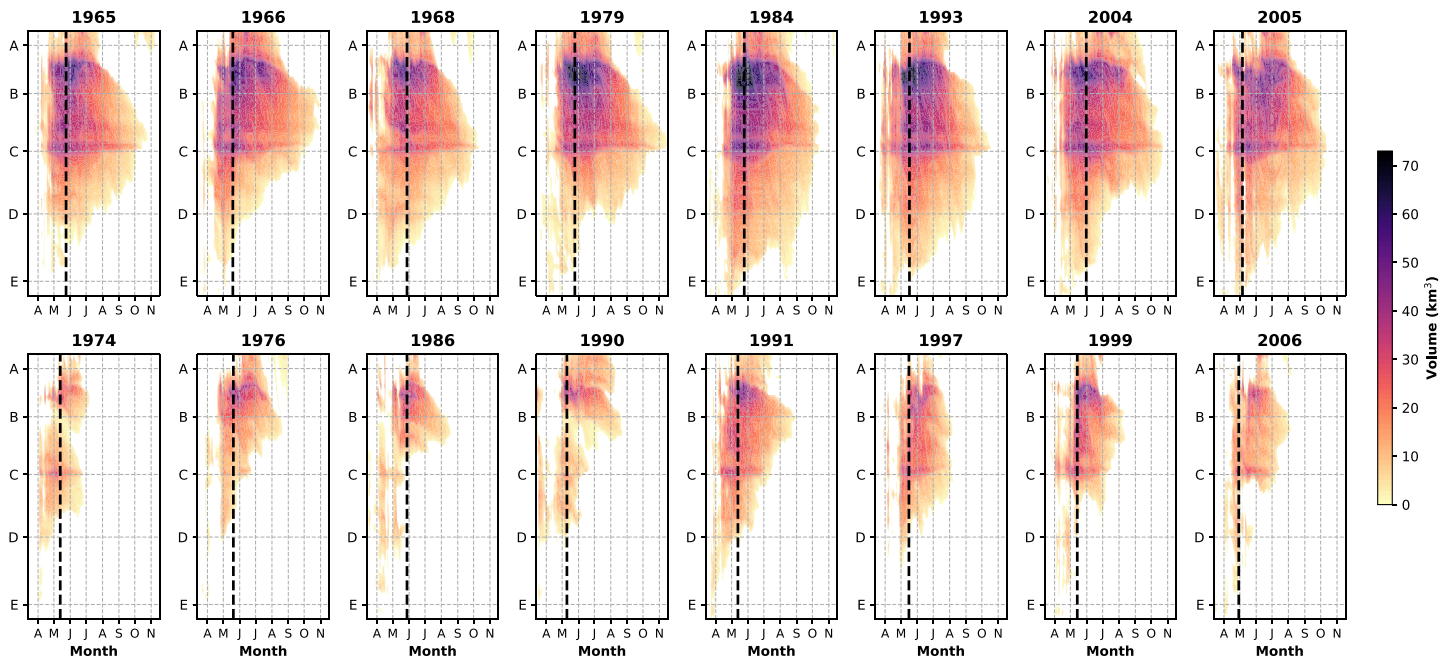
Figure 6. Comparison of along-shelf distribution of the Cold Pool volume (km^3) between strong (upper eight panels) and weak (lower eight panels) Cold Pool years. In each panel, x axis represents time during a year from early March to end of November, and y axis represents the along-shelf geographical locations, from A—Nantucket Shoals, B—Montauk Point, C—Sandy Hook, D—Delaware Bay, and E—Chesapeake Bay (Figure 1). The x and y axis are fixed for each panel. The black thick dashed line in each panel represents the time when peak total volume is obtained for each particular year.

In this study, we categorize all 50 Cold Pool events into three types: strong, normal, and weak Cold Pool years based on the CPI. Those years whose CPI are above one STD are regarded as strong Cold Pool years, and those below one negative STD are regarded as weak Cold Pool years. There are eight strong Cold Pool years (1965, 1966, 1968, 1979, 1984, 1993, 2004, and 2005) and eight weak years (1974, 1976, 1986, 1990, 1991, 1997, 1999, and 2006) during the 50 years (Figure 5e). The rest of the years are considered as normal years.

By definition, the CPI is using not only temperature as a selection criterion but also its expansion volume and the persistence time. The CPI is highly correlated with the annual mean Cold Pool, core temperature, persistence, and annual time-integrated volume ($r = -0.77$, -0.78, -0.80, and 0.94, respectively; both $p < 0.05$). Thus, the CPI is representative of the strength of Cold Pool events.

3.4. Strong and Weak Cold Pool Events

To further investigate the year-to-year differences in the Cold Pool events, we select extreme years (strong and weak Cold Pool years) and compare their spatiotemporal variations in the Cold Pool volume and temperature as well as their southwestward propagation during the summer months.
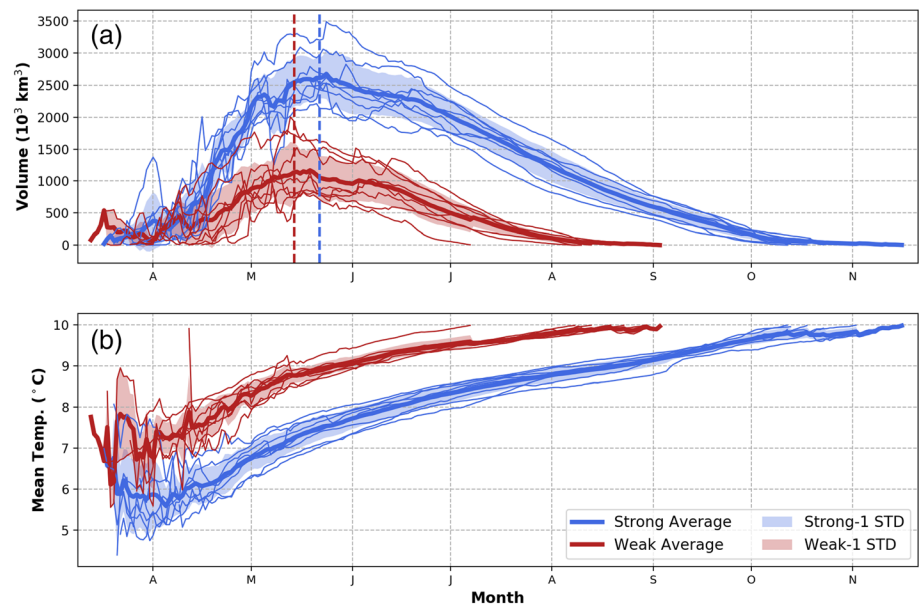
3.4.1. Volume and Temperature

Seasonal variations of the Cold Pool volume and temperature along the shelf differ significantly between strong and weak Cold Pool years (Figures 6 and 7). Although there are slight differences among the strong years, the maximum volume is located over the NES, between location A—Nantucket Shoals and B—Montauk Point (Figure 6), which is consistent with the 50-year climatological case presented in Chen et al. (2018). The along-shelf distribution of the Cold Pool minimum temperature for all the strong years suggests that it is also the location where the coldest Cold Pool water originates (Figure 7). This is consistent with previous findings that the spring cold water located over the NES near the Nantucket Shoals is the main source of water for the Cold Pool (Chen et al., 2018; Houghton et al., 1982).

The weak Cold Pool years have not only a shrinking volume but also increasing temperature along the shelf when comparing to strong years (Figures 6 and 7). The maximum Cold Pool volume in the along-shelf direction is still located over the NES, between location A and B; however, the values is only about a half of that
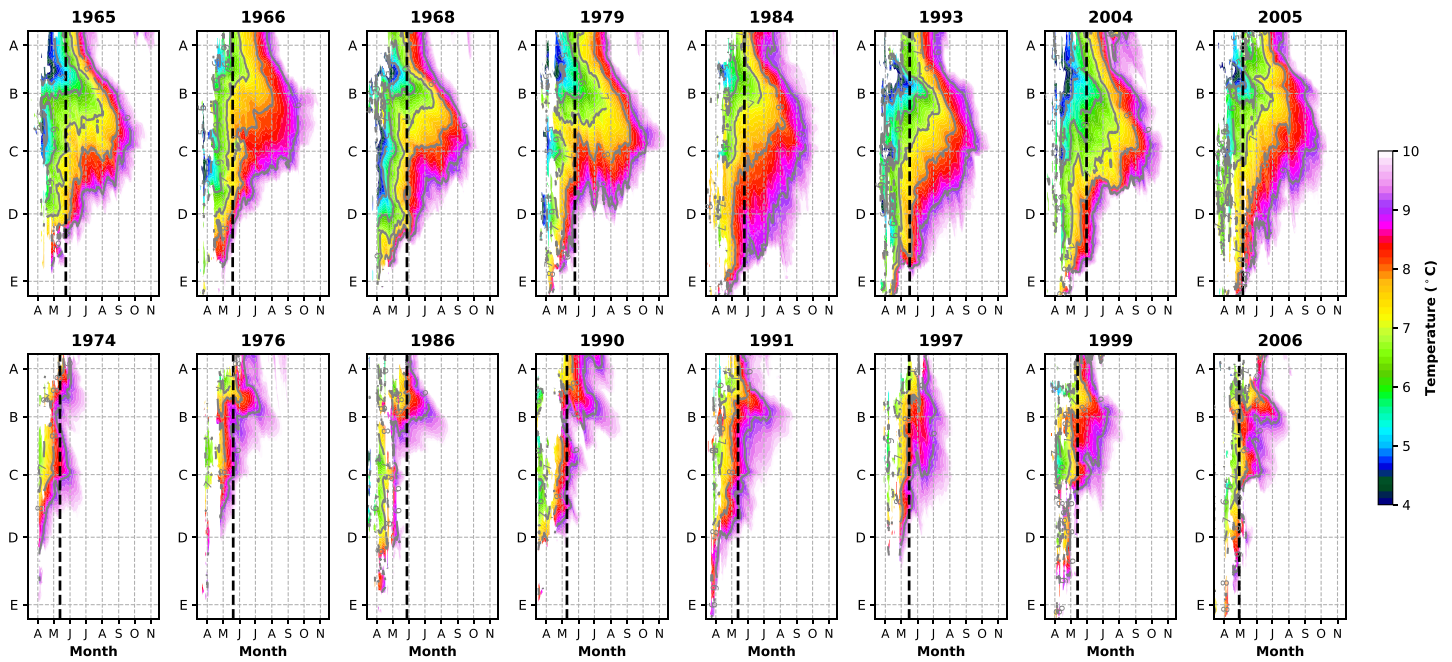
Figure 7. Same as Figure 6 but for minimum temperature of the Cold Pool. Temperature contours in 5, 6, 7, 8, and 9°C are plotted as gray solid lines in each panel.

for the strong years (Figure 8a). In addition, in the southern MAB region (south of location C—Sandy Hook), south of the HSV, there is almost no Cold Pool water after the volume peaks in the weak years. Similarly, the coldest Cold Pool water is still located over the NES, but its average temperature is about 2°C warmer than that in strong years (Figure 8b). After the volume peaks, Cold Pool temperatures in weak years are nearly above 8°C along the whole shelf (Figure 7).

Figure 8. Comparison of seasonal time series of the Cold Pool total volume, mean temperature, and core propagation trajectory between strong (blue) and weak (red) years. (a) The seasonal time series of Cold Pool volume of the strong years (blue thin lines) and the weak years (red thin lines), with their respective mean values (thick lines) and one STDs (shaded area). The vertical dashed lines represent average peak day of strong and weak years. (b) Same as (a) but for the Cold Pool mean temperature.
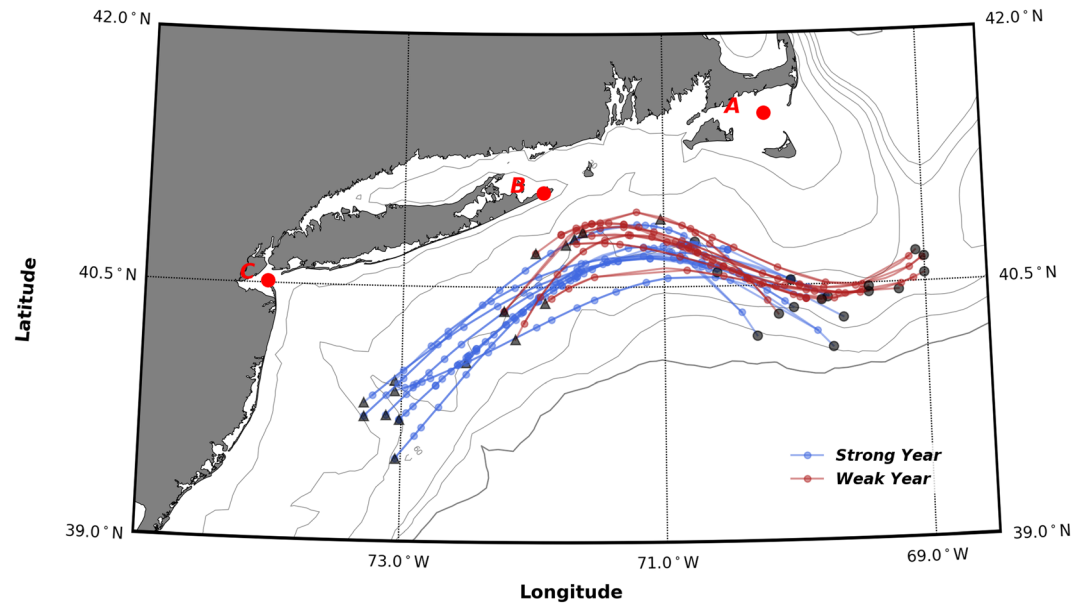
Figure 9. Cold Pool core trajectories during the summer of strong (blue) and weak (red) Cold Pool years. Black circles represent the start points of the trajectories, and black triangles represent the end points. Bathymetry of the Mid-Atlantic Bight are given (gray solid lines) in 20, 40, 60, 80, 100, and 200 m.

3.4.2. Persistence and Warming Rates

The Cold Pool initiates and peaks at nearly the same time (difference ~8 days) during the strong and weak Cold Pool years (Figure 8a). However, the persistence time is about 7 months on average (216 days) for the strong years and only about 4.5 months on average (138 days) for the weak years. Although the Cold Pool temperature is about 2°C warmer in the weak years (Figure 8b), the warming rate of the whole water mass is almost the same before the volume peak for strong and weak years (1.21 and 1.26°C/month, respectively). After the volume peaks, the warming rates decrease to about 0.43 and 0.33°C/month for strong and weak years.

3.4.3. Core Propagation Trajectory

One of the distinctive features of the Cold Pool is the southwestward propagation of the core during the summer. The Cold Pool core travels along the 60- to 80-m isobaths during all the strong and weak years (Figure 9). During the strong years, the southward propagation path of the Cold Pool Core usually begins in the NES in the early spring and disappears near the HSV (location C) in the fall (Figure 8c). However, during the weak years, the average location of the Cold Pool cores has a northward shift, and the cores usually disappear off Montauk Point (location B) instead of HSV (location C).

4. Interannual Temperature Budget of the CPR

In order to investigate the difference in the heat balance between strong and weak years, we compute the volume-averaged heat budget of the near-bottom (below 30 m depth) control volume over the CPR (Figure 1). We select the same CPR as that in Chen et al. (2018), covering the midshelf and outer shelf of the NES, northern and southern New York Bight, between the 40- and 100-m isobaths. For the near-bottom control volume CPR, its volume-averaged temperature balance can be written as

$$
\underbrace{<\frac{\partial T}{\partial t}>}_{T_{trend}} = \underbrace{<K_v\frac{\partial^2 T}{\partial z^2}>}_{V_{dif}} + \underbrace{\overbrace{<-\boldsymbol{u}\cdot\nabla T>}^{H_{adv}} + \overbrace{<-w\frac{\partial T}{\partial z}>}^{V_{adv}}}_{T_{adv}} + \underbrace{<K_h\nabla^2 T>}_{H_{dif}},
\tag{2}
$$

where $T = T(x,y,z,t)$ represents temperature, $\boldsymbol{u}$ represents horizontal velocity, w is the vertical velocity, and
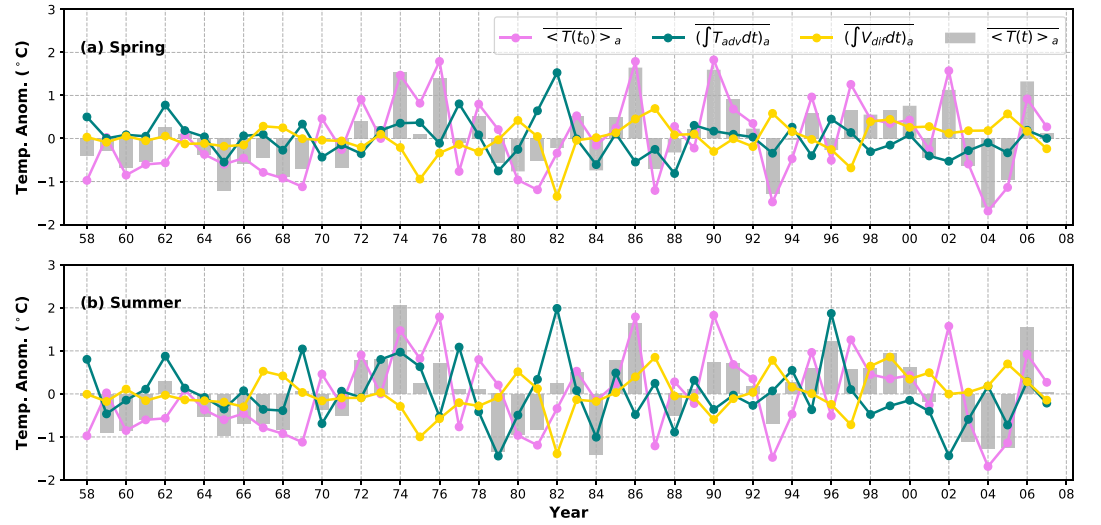
Figure 10. Interannual variability of the volume-averaged temperature anomaly budget terms of Equation 5 during the spring (a; April–May–June) and summer (b; July–August–September): the initial temperature anomaly at time t_0 (CD 86; purple lines) (end of March) of each year, the cumulative temperature anomaly due to total advection (green lines) and vertical diffusion (yellow lines), and the mean temperature anomaly of the near-bottom CPR during spring and summer (gray bars).

K_v and K_h represent vertical and horizontal diffusion coefficient (m²/s). The symbol $<>$ is the volume average operation, which could be expressed as $<> = \frac{1}{V}\iint\left(\int_{\eta}^{\xi_{30}} dz\right) dxdy$, where V represents the total volume of the CPR, η represents the physical bottom, and ξ_{30} refers to the 30-m depth separating the surface and near-bottom layers.

The volume-averaged heat budget equation states that time rate of temperature change of the CPR (T_{trend}) is balanced by the vertical temperature diffusion (V_{dif}, which contains penetrating solar radiation), horizontal (H_{adv}) and vertical (V_{adv}) temperature advection, and horizontal diffusion (H_{dif}). Time integral of Equation 2 could be expressed as

$$\int_{t_0}^{t} T_{trend}dt = \int_{t_0}^{t} V_{dif}dt + \int_{t_0}^{t} T_{adv}dt + \int_{t_0}^{t} H_{dif}dt, \tag{3}$$

where t_0 is the initial time. The horizontal diffusion term could be omitted and considered as a residual (much smaller than the other terms). Equation 3 could be further expressed as

$$<T(t)> = <T(t_0)> + \int_{t_0}^{t} V_{dif}dt + \int_{t_0}^{t} T_{adv}dt, \tag{4}$$

which states that the volume-averaged temperature of the CPR at time t is contributed by the volume-averaged initial temperature and the time integral of vertical temperature diffusion and total advection from t_0 to t. The initial time t_0 is set to be the average onset date of all 50 years, which is CD 86 (26 March). Our analysis is focused on the Cold Pool season only, which is from the initial time CD 86 (26 March) to CD 270 (26 September).

We first examined the heat budget terms in spring (April–May–June) and summer (July–August–September). Anomalies of each term in Equation 4 are calculated by removing the seasonal climatology of all 50 years:

$$<T(t)>_a = <T(t_0)>_a + \left(\int_{t_0}^{t} V_{dif}dt\right)_a + \left(\int_{t_0}^{t} T_{adv}dt\right)_a. \tag{5}$$

Temporal averages of the anomalies are performed within each season (spring, summer, or the whole Cold Pool season). Therefore, Equation 5 can be expressed as
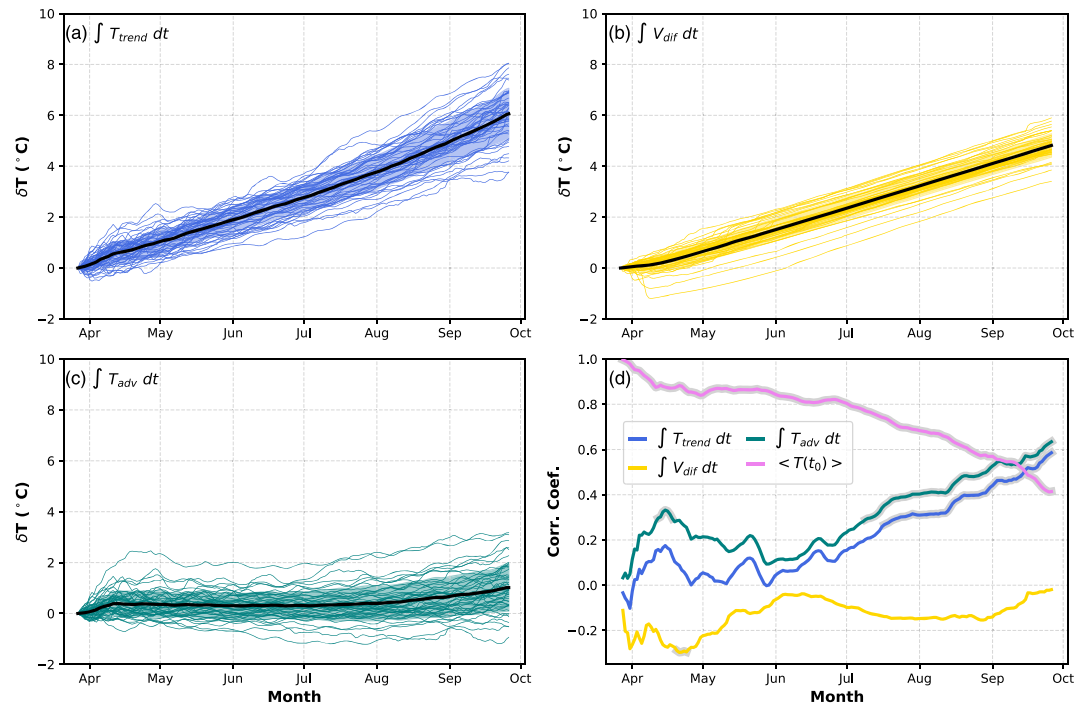
Figure 11. Fifty-year seasonal time series of the time-integrated (since the average Cold Pool onset date—CD 86 (end of March)) volume-averaged temperature budget terms of the CPR and their correlations with the CPR volume-averaged temperature, from CD 86 (end of March) to the average end date—CD 269 (end of September). (a–c) The time integral of volume-averaged temperature terms of Equation 3 for all 50 years: time rate of temperature change of the CPR (a; $\int_{t_0}^{t} T_{trend}\mathrm{d}t$; blue), vertical temperature diffusion (b; $\int_{t_0}^{t} V_{dif}\mathrm{d}t$; yellow), and total temperature advection (c; $\int_{t_0}^{t} T_{adv}\mathrm{d}t$; green). The black thick line in each panel represents the 50-year mean time series, and the shade represents the respective one STD. The rest of the color lines represent all 50 individual years. (d) The correlation between the volume-averaged temperature of the CPR ($<T(t)>$) and the time-integrated volume-averaged temperature terms in (a)–(c) and the initial CPR temperature at CD 86 ($<T(t_0)>$; purple) during the 50 years (1958–2007). Correlations that are significant at the 95% confidence level are thickened in light gray.

$$\overline{<T(t)>_a} = \overline{<T(t_0)>_a} + \overline{\left(\int_{t_0}^{t} V_{dif}\mathrm{d}t\right)_a} + \overline{\left(\int_{t_0}^{t} T_{adv}\mathrm{d}t\right)_a}. \tag{6}$$

The spring and summer temperature anomalies of the near-bottom CPR have similar interannual variations ($r = 0.84$, $p < 0.05$; Figure 10). Both of which are significantly correlated with the initial temperature anomalies, although the correlation coefficient drops from 0.90 in spring to about 0.65 in summer (both $p < 0.05$). The temperature anomalies caused by the total advection also have consistent interannual variations during spring and summer ($r = 0.85$, $p < 0.05$). Their correlation with the CPR temperature anomaly increases from 0.11 ($p > 0.05$) in spring to 0.41 ($p < 0.05$) in summer. Similarly, the temperature anomalies caused by the vertical diffusion have nearly the same interannual variability during spring and summer ($r = 0.96$, $p < 0.05$). However, neither spring nor summer vertical diffusion is correlated with the interannual change of the CPR temperature anomaly ($r = -0.18$ and -0.14, respectively; both $p > 0.05$).

To investigate the relative importance of the initial temperature, vertical diffusion, and total advection during the Cold Pool seasons, we examined the time integral of each term in Equation 4 on interannual time-scales. As shown in Figure 11a, the time integral of the temperature trend term ($\int_{t_0}^{t} T_{trend}\mathrm{d}t$), starting with the Cold Pool onset, has an almost linear increase indicative of the near-bottom warming during the Cold Pool season. The average temperature increase reaches about 6.06°C (Figure 11a). Comparing with the total advection, the vertical temperature diffusion contributes most of temperature increase of the near-bottom CPR, the time integral of which also increases linearly to about 4.82°C by the end of the Cold Pool season (Figure 11b). The total advection only contributes to a temperature change of about 1.02°C, and the
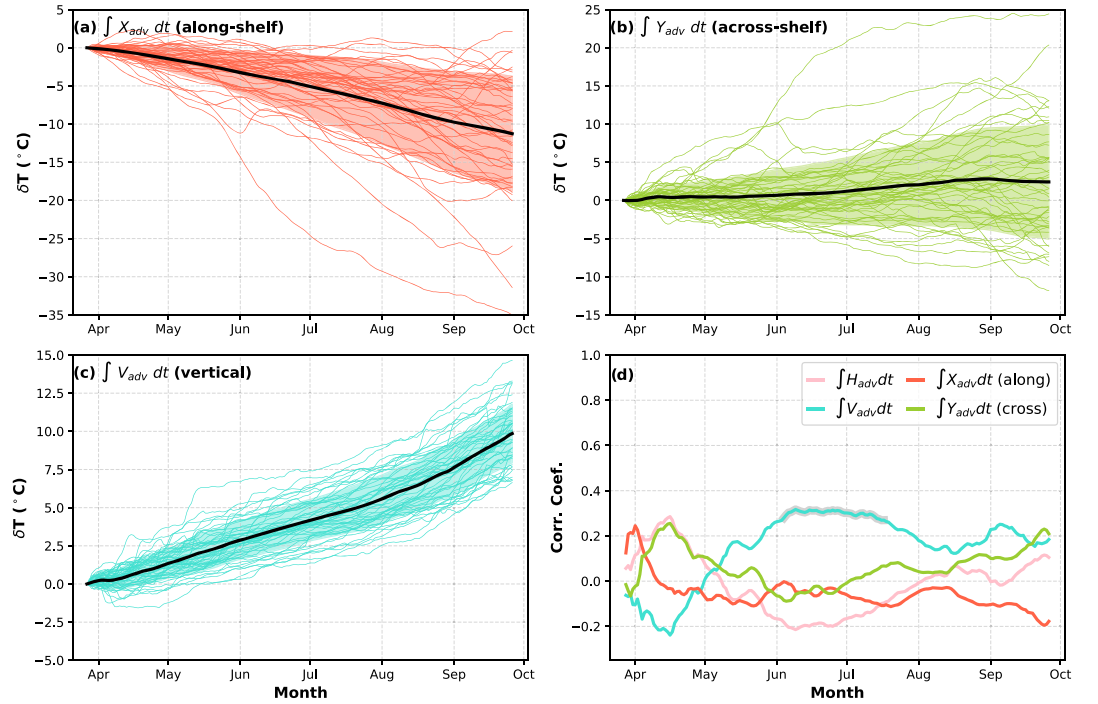
Figure 12. Similar as Figure 11 but for the time integral of volume-averaged (a) along-shelf ($\int_{t_0}^{t} X_{adv}\mathrm{d}t$; light red), (b) across-shelf ($\int_{t_0}^{t} Y_{adv}\mathrm{d}t$; light green), and (c) vertical ($\int_{t_0}^{t} V_{adv}\mathrm{d}t$; light blue) temperature advection. (d) The correlation between the volume-averaged temperature of the CPR ($<T(t)>$) and the time-integrated volume-averaged temperature advection terms in (a)–(c) and the horizontal temperature advection ($\int_{t_0}^{t} H_{adv}\mathrm{d}t$; pink) during the 50 years (1958–2007). Correlations that are significant at the 95% confidence level are thickened in light gray.

temperature increase happens mainly in the late summer (August), before which it remains at almost the same value since mid-April (Figure 11c).

Although the vertical temperature diffusion contributes most of the temperature increase in the near-bottom CPR, the correlation between the time series of volume-averaged CPR temperature ($<T(t)>$) and the temperature change caused by vertical diffusion ($\int_{t_0}^{t} V_{dif}\mathrm{d}t$) is very low (between -0.35 and 0) throughout the Cold Pool seasons and is only significant during a short period of time at the end of April (Figure 11d). However, the correlation with the temperature change due to the total advection gradually increases from the beginning of summer (June) and becomes significant at the 95% confidence level during the summer and until the end of the Cold Pool season (Figure 11d). The time integral of temperature trend has similar behavior but with slightly lower correlation coefficients.

The total advection can be separated into three components/directions: along-shelf, across-shelf, and vertical, as expressed by the equation:

$$\int_{t_0}^{t} T_{adv}\mathrm{d}t = \underbrace{\int_{t_0}^{t} X_{adv}\mathrm{d}t}_{along-shelf} + \underbrace{\int_{t_0}^{t} Y_{adv}\mathrm{d}t}_{across-shelf} + \underbrace{\int_{t_0}^{t} V_{adv}\mathrm{d}t}_{vertical}. \tag{7}$$

Therefore, Equation 4 could be re-expressed as

$$<T(t)> \ = <T(t_0)> + \int_{t_0}^{t} V_{dif}\mathrm{d}t + \int_{t_0}^{t} X_{adv}\mathrm{d}t + \int_{t_0}^{t} Y_{adv}\mathrm{d}t + \int_{t_0}^{t} V_{adv}\mathrm{d}t. \tag{8}$$

During the Cold Pool season, the along-shelf advection provides a cooling effect to the near-bottom temperature of the CPR ($\delta T = -11.26$°C by the end of Cold Pool season), mainly compensating with the warming from the vertical temperature advection ($\delta T = 9.85$°C; Figures 12a and 12c). The temperature change due
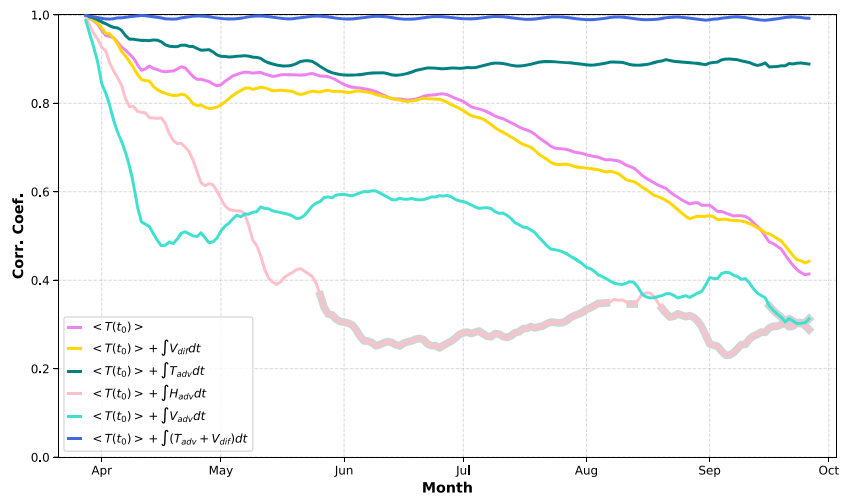
Figure 13. The correlation coefficients between the volume-averaged temperature of the CPR ($<T(t)>$) and its initial temperature ($<T_0(t)>$) combinations as indicated in the lower left legend. Correlations that are below the 99% significance level are thickened in light gray.

to across-shelf advection ($\delta T = 2.42°C$) is much smaller than the other two advection terms (Figure 12b). Both along- and across-shelf advection have a relatively larger interannual variation than the vertical advection.

Further correlation analysis between the time series of volume-averaged CPR temperature ($<T(t)>$) and the horizontal and vertical advection terms ($\int_{t_0}^{t} H_{adv} dt, \int_{t_0}^{t} V_{adv} dt$) suggests that the horizontal temperature advection does not have as significant a correlation as the total advection, and the vertical advection is only significantly correlated during the first half of the summer (June to mid-July; Figure 12d). Neither along-shelf nor across-shelf temperature advection is significantly correlated with the CPR near-bottom temperature.

Differing from the diffusion and advection terms, the correlation between the volume-averaged CPR temperature ($<T(t)>$) and its initial temperature ($<T(t_0)>$) stays high and robust throughout the Cold Pool season (Figure 11d). This suggests that the initial temperature is the most important factor in impacting the Cold Pool temperature on interannual timescales. The correlation coefficients decrease gradually but remain above 0.8 during the spring (by the end of June). As the summer progresses, the coefficients drop more quickly and reach below 0.6 by the end of August and around 0.4 by the end of the Cold Pool season.

Adding the vertical temperature diffusion term does not significantly change the decreasing correlation obtained from $<T(t_0)>$ by itself during the summer (Figure 13). Rather, it is the total advection term that largely increases the overall correlation, especially in the summer months. Although the correlation with the combination of initial temperature and total advection has a slight decrease to about 0.86 by the end of May, it remains consistent at about 0.89 for 4 months until the end of the Cold Pool season (Figure 13). In comparison, the combinations of initial temperature and horizontal or vertical advection do not yield as high and robust correlations as does the total advection. Therefore, the interannual variability of the near-bottom CPR temperature can be better represented by the combination of the initial temperature of the Cold Pool at its formation and the total temperature advection.

Nevertheless, the relative importance of the total advection versus vertical diffusion varies from year to year. We examine further the temperature anomaly budget of the near-bottom CPR during the extreme (strong and weak) Cold Pool years (Figure 14), following Equation 5. The initial temperature has been added to both of the cumulative temperature anomalies due total advection and vertical diffusion, in order to compare with the time series of the CPR temperature anomalies. For both the strong and weak years, the seasonal fluctuation of the CPR temperature anomaly is more likely to be closely related with that of the temperature anomaly due to the total advection of temperature. The correlations with the temperature anomalies due to total advection are all above 0.8 for the strong years, except in 1968, and all above 0.6 for the weak years with the exception of 1999.
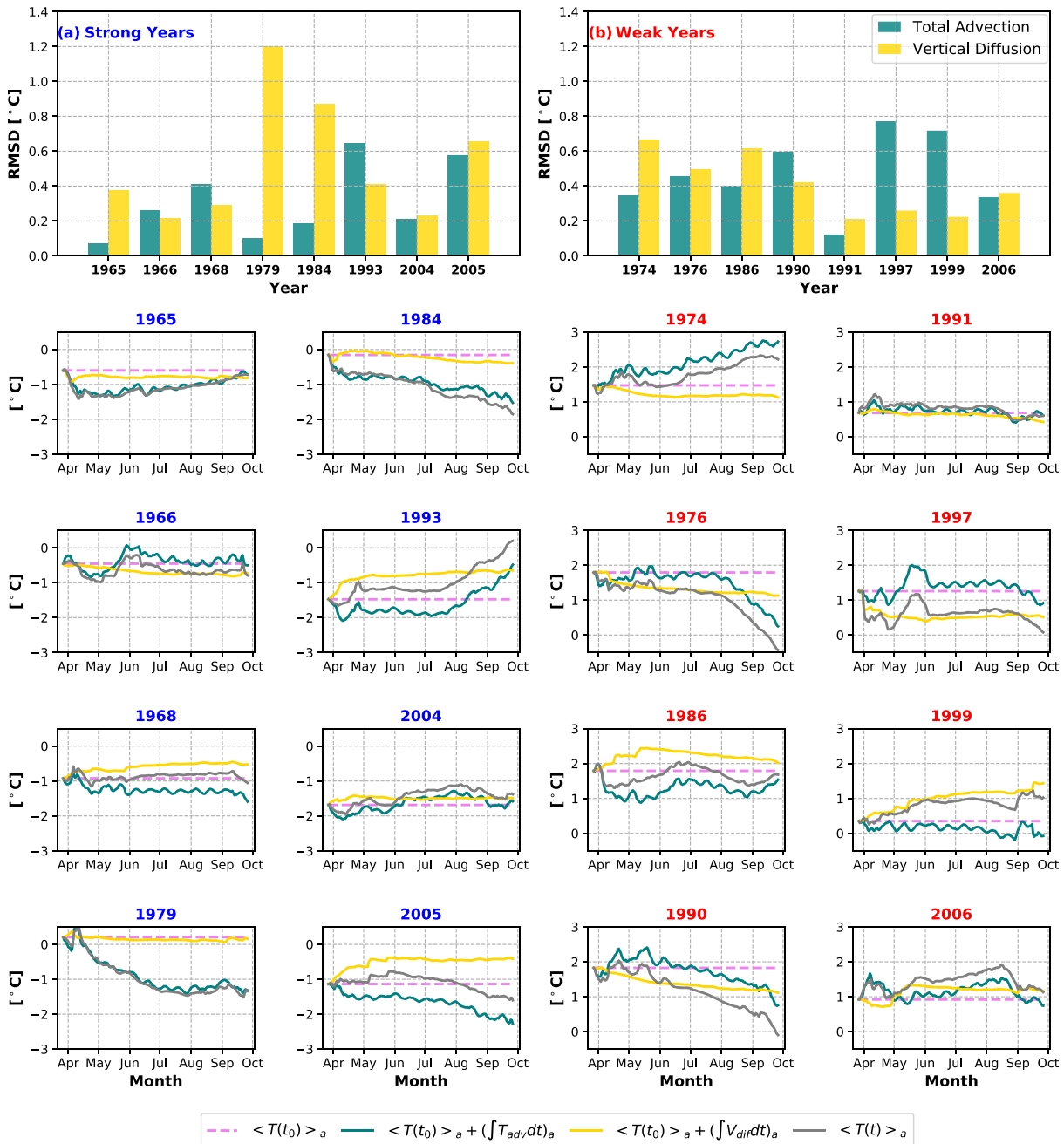
Figure 14. The relative importance of total advection versus vertical temperature diffusion in controlling the near-bottom CPR temperature anomalies and their seasonal evolution in the strong and weak Cold Pool years. (a and b) The RMSD between the temperature anomaly ($<T(t)>_a$) and that due to total advection ($<T(t_0)>_a + \left(\int_{t_0}^{t} T_{adv} dt\right)_a$; green bars)/vertical diffusion ($<T(t_0)>_a + \left(\int_{t_0}^{t} V_{dif} dt\right)_a$; yellow bars), only for the eight (a) strong and (b) weak Cold Pool years. The rest of the panels show the evolution of cumulative temperature anomaly budget terms for each strong (blue subtitles) and weak (red subtitles) year, following Equation 5. The initial temperature anomaly has been added to the time series of cumulative temperature anomaly due to total advection and vertical diffusion, in order to compare with the temperature anomaly time series of the CPR.

The root-mean-square deviation (RMSD) between the CPR temperature anomalies and those due to total advection is much smaller than that due to vertical diffusion in the strong years of 1965, 1979, and 1984, suggesting that the total temperature advection works as a dominant factor in impacting the seasonal evolution of the near-bottom CPR temperature anomalies. The RMSD with temperature anomalies due to total advection is less than 0.2 for these three strong years. For the rest of the strong years, the RMSDs with temperature
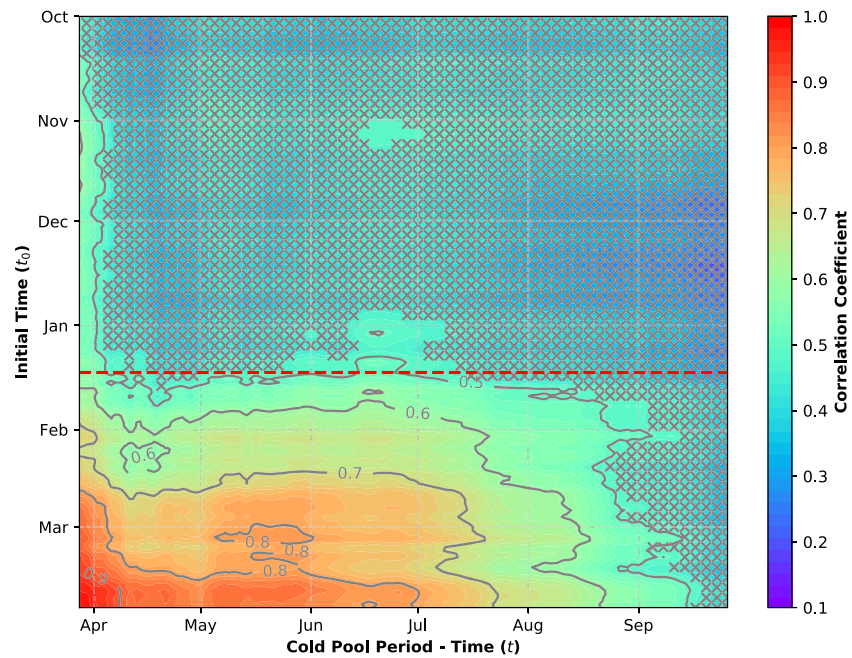
Figure 15. The correlations between the changing initial temperatures and temperature of the CPR during the Cold Pool period. The initial time t_0 ranges from last year's October to this year's March before the Cold Pool onset. The x axis represents the Cold Pool season from CD 86/end of March to CD 269 (end of September). Correlations that are significant below the 99.9% confidence level are masked (gray crosses). The contours of coefficients from 0.5 to 0.9 are plotted as gray solid lines. The red dashed line represents the correlation boundary since mid-January.

anomalies due to total advection are comparable with those due to vertical diffusion. This suggests that it is the combination of the total advection and vertical diffusion that ultimately controls the seasonal evolution of temperature anomalies.

For the weak Cold Pool years of 1997 and 1999, the RMSDs between the temperature anomalies of the near-bottom CPR and those due to vertical diffusion are much smaller than the component due to total advection, suggesting that the vertical diffusion outweighs total advection in controlling the seasonal evolution of temperature anomalies. For the rest of the five weak years, except 1990, the RMSD values with temperature anomalies due to total advection are smaller but comparable to those due to vertical diffusion. This implies that total advection works as the main factor contributing to the evolution of temperature anomalies during the Cold Pool season, with vertical diffusion also influencing the CPR characteristics. Both of vertical diffusion and the total advection are important in determining the temperature evolution in the weak year 1990, with vertical diffusion dominating.

5. Discussion and Summary

The near-bottom temperature variability on the MAB shelf is linked to a wide range of phenomena from commercially important fisheries to hurricane prediction (Coakley et al., 2016; Miller et al., 2016; Nye et al., 2011; Sullivan et al., 2005). Chen et al. (2018) investigated the seasonal variability of the Cold Pool characteristics and found that vertical diffusion contributes most of the near-bottom temperature warming during the Cold Pool season. However, it is oceanic advection that dominates the spatial warming pattern of the near-bottom layer over the shelf. In this study, we extended the Chen et al. (2018) work and investigated the interannual variability of the Cold Pool with regard to its persistence, volume, and temperature, all of which exhibit significant differences from year to year.

A heat budget analysis of the near-bottom CPR suggested that temperature anomaly during the stratified seasons can be impacted by the initial temperature at the beginning of the Cold Pool season, the temperature anomaly due to vertical temperature diffusion and total oceanic advection. The interannual variability of the near-bottom Cold Pool temperature is mainly associated with the initial temperature during the spring. The

analysis shows that the temperature of the previous cold season (winter) from mid-January to the end of March is strongly correlated with the near-bottom CPR temperature anomaly during the stratified seasons. Figure 15 shows the correlations between the initial temperatures on CD 86 (end of March) back to the preceding October (*y* axis) and the near-bottom temperature during the Cold Pool season (*x* axis). The near-bottom temperatures before mid-January are not significantly correlated with the temperature anomalies during the Cold Pool season. After mid-January, the average correlation between the initial temperature and temperature during the Cold Pool season gradually increases with time toward the onset of the Cold Pool event. Therefore, we conclude that the winter (mid-January to March) temperature anomaly is the primary factor in determining the interannual variability of the near-bottom CPR temperature anomaly during the stratified seasons, in particular during spring. Chen et al. (2016) reached a similar conclusion after investigating the interannual variability of winter-spring temperature over the MAB during 2003–2014, which stated that the depth-mean winter temperature anomaly is an indicator of the spring temperature anomaly and the winter temperature is mainly controlled by the initial temperature at the end of fall and the air-sea heat fluxes. These strong correlations between seasons imply the long persistence of the near-bottom temperature anomaly from winter to summer, which suggests the possibility of seasonal predictability of the near-bottom CPR temperature.

Chen et al. (2016) also found that the mean winter/spring temperature is better described by the initial temperature of the season and the mean cumulative air-sea heat flux. However, for the near-bottom layer (below 30 m), our analysis suggests that spring/summer temperature anomaly is better represented by the initial temperature anomaly and the total oceanic advection (as shown in Figure 13). Although vertical diffusion has a large impact on the mean temperature change of the CPR during the Cold Pool season, it contributes considerably less to the interannual temperature variability (Figure 11), relative to the other two terms in the heat budget equation. This is mainly associated with the relative uniformity of the penetrated heat flux into the near-bottom layer on the interannual timescale. However, for some particular years, vertical diffusion can have a dominant role in impacting the annual temperature variation of the CPR—for example, years 1997 and 1999 (Figure 14). We also note that Chen et al. (2016) focus on the depth-mean temperature, rather than separating the surface and near-bottom layers as was done here. Unlike the surface, the near-bottom temperature does not feel a direct impact from air-sea heat fluxes during the Cold Pool season as a result of the strong stratification. In the spring (April–June), stratification is almost fully developed over the MAB continental shelf, and surface temperatures remain trapped in the surface layer until the fall mixing events.

Thus, we conclude that the combination of initial temperature and total oceanic advection outweighs the contribution from vertical diffusion in the summer (Figure 13). On interannual timescales, the spring and summer temperature anomaly is strongly correlated with the combination of initial temperature and total oceanic advection, with the robust correlation coefficient of about 0.89. This high correlation identifies the importance of oceanic advection processes in determining the near-bottom temperature anomaly. This is largely consistent with the conclusions from Shearman and Lentz (2010), which pointed out that the temperature changes over the whole NWA continental shelf is controlled by the along-shelf advection, associated with the equatorward coastal current system from Labrador to Cape Hatteras, rather than local air-sea heat exchanges. Detailed analysis about the selected strong and weak Cold Pool years also highlights the dominance of the total oceanic advection with the exception of two extremely weak Cold Pool years, 1997 and 1999, when the vertical diffusion plays a more important role.

We note that the model has a slight warm bias in both SST and BT relative to observations (section 2.2), with a pattern suggesting that it underestimates the vertical stratification in the water column. Stronger stratification would imply a diminished role for vertical temperature diffusion and advection to the near-bottom layer. This reinforces the main conclusion that the near-bottom temperature anomaly during the Cold Pool season is dominated by the initial temperature and the total advection. On seasonal timescales, along-shelf advection provides a cooling effect to the near-bottom CPR temperature, largely balanced by warming due to vertical advection and to a lesser extent by a slight warming due to cross-shelf advection (Figures 12a–12c). It is worth noting that the simple model that Shearman and Lentz (2010) used is for the depth-mean flat-bottom shelf and does not consider the cross-shelf advection. On interannual timescales, our analysis suggests that the cross-shelf advection term has the largest variability among all the

advection terms (Figure 12b). The large interannual variability of the cross-shelf advection is associated with the shelf-slope heat exchange processes at the shelf break, for example, the onshore intrusion of the warm-core rings and Gulf Stream water masses (Gawarkiewicz et al., 2012, 2018; Zhang & Gawarkiewicz, 2015).

The 50-year (1958–2007) model simulation of the northeast U.S. continental shelf provides a sufficiently long record to analyze the trends in the MAB Cold Pool. Results suggest that the Cold Pool persistence time has a decreasing trend of about -6.60 ± 2.83 days/decade. Both the time-integrated and peak Cold Pool volume have weak decreasing trends of about -4459.60 ± 6354.25 and -9.06 ± 53.83 km^3/decade, respectively. At the same time, both the initial and annual mean temperature of the Cold Pool water mass have generally increasing trends of about 0.15 ± 0.10 and 0.05 ± 0.03°C/decade throughout the time series (1958–2007). For the near-bottom CPR temperature, its long-term trend during 1958–2007 is about 0.12 ± 0.08°C/decade for the Cold Pool season, which warms faster than the SST as estimated by Shearman and Lentz (2010) based on observations during 1875–2007 (0.07 ± 0.03°C/decade) but slower than the bottom warming estimated by Kavanaugh et al. (2017) during 1982–2014 (0.2–0.4°C/decade). The Cold Pool strength as represented by the CPI derived in this paper has a decreasing trend of about -0.11 ± 0.10/decade. Understanding of the long-term warming in the near-bottom layer and its ecological implications warrants further investigation and is beyond the scope of this paper.

The temperature budget analysis confirms the important roles of the initial temperature and total advection not only for interannual variability but also for longer term trends. The linear trend in the initial temperature of the near-bottom CPR has about the same value as that of the near-bottom CPR temperature during the Cold Pool season (0.12 ± 0.09°C/decade). However, the temperature change due to total advection has a decreasing trend of about -0.06 ± 0.04°C/decade in the spring and about -0.08 ± 0.07°C/decade in the summer. The vertical temperature diffusion from the surface layer balances the total advection, which has almost the exact opposite long-term trend with those of the total advection in the spring and summer.

Decadal variability of the Cold Pool has also been suggested in this look at the interannual Cold Pool characteristics, which highlights the complexity of the near-bottom shelf circulation system of the MAB. A better understanding of the local atmospheric and near-bottom oceanic processes and their linkages to the large-scale climate system and circulation, for example, trends in the meridional shift of the Gulf Stream position (Gawarkiewicz et al., 2012; Joyce et al., 2019), the Atlantic Meridional Oscillation (Enfield et al., 2001; Kerr, 2000), and the North Atlantic Oscillation (Hurrell & Deser, 2010), will be paramount for improved predictions and understanding implications from fisheries to hurricanes in this region.

Data Availability Statement

Model simulations are available at the Earth System Modeling Lab website at Rutgers (http://esm.rutgers.edu) as well as through Figshare (https://doi.org/10.6084/m9.figshare.12648896.v1). The bottom trawl survey data calibrated by NEFSC is available at the website (http://comet.nefsc.noaa.gov/cgi-bin/ioos/ioos.pl). The gridded observational surface and bottom temperature along the continental shelf off the Canadian and U.S. East Coasts (Richaud et al., 2016) are available at the website (https://www2.whoi.edu/staff/ykwon/data/).

References

Bi, H., Ji, R., Liu, H., Jo, Y. H., & Hare, J. A. (2014). Decadal changes in zooplankton of the northeast US continental shelf. *PLoS ONE*, *9*(1), e87720. https://doi.org/10.1371/journal.pone.0087720

Bigelow, H. B. (1933). Studies of the waters on the continental shelf, Cape Cod to Chesapeake Bay. I. The cycle of temperature. *Papers in Physical Oceanography and Meteorology*, *2*(4), 1933-12.

Brown, W. S., Schofield, O., Glenn, S., Kohut, J., & Boicourt, W. (2015). The mid-Atlantic autumn cold pool during GliderPalooza-2013. In *OCEANS 2015-MTS/IEEE Washington* (pp. 1-10). https://doi.org/10.23919/OCEANS.2015.7401814

Chen, K., Kwon, Y. O., & Gawarkiewicz, G. (2016). Interannual variability of winter-spring temperature in the Middle Atlantic Bight: Relative contributions of atmospheric and oceanic processes. *Journal of Geophysical Research: Oceans*, *121*, 4209–4227. https://doi.org/10.1002/2016JC011646

Chen, Z., Curchitser, E., Chant, R., & Kang, D. (2018). Seasonal variability of the cold pool over the Mid-Atlantic Bight Continental Shelf. *Journal of Geophysical Research: Oceans*, *123*, 8203–8226. https://doi.org/10.1029/2018JC014148

Coakley, S. J., Miles, T., Kohut, J., & Roarty, H. (2016). Interannual variability and trends in the Middle Atlantic Bight cold pool. In *OCEANS 2016 MTS/IEEE Monterey* (pp. 1–6). https://doi.org/10.1109/OCEANS.2016.7761184

Enfield, D. B., Mestas-Nuñez, A. M., & Trimble, P. J. (2001). The Atlantic multidecadal oscillation and its relation to rainfall and river flows in the continental US. *Geophysical Research Letters*, *28*(10), 2077–2080. https://doi.org/10.1029/2000GL012745

Fairbanks,, R. G. (1982). The origin of continental shelf and slope water in the New York Bight and Gulf of Maine: Evidence from $H_2^{18}O$/$H_2^{16}O$ ratio measurements. *Journal of Geophysical Research*, *87*(C8), 5796–5808. http://dx.doi.org/10.1029/jc087ic08p05796

Flagg, C. N., Wirick, C. D., & Smith, S. L. (1994). The interaction of phytoplankton, zooplankton and currents from 15 months of continuous data in the Mid-Atlantic Bight. *Deep Sea Research Part II: Topical Studies in Oceanography*, *41*(2–3), 411–435. https://doi.org/10.1016/0967-0645(94)90030-2

Forsyth, J. S. T., Andres, M., & Gawarkiewicz, G. G. (2015). Recent accelerated warming of the continental shelf off New Jersey: Observations from the CMV Oleander expendable bathythermograph line. *Journal of Geophysical Research: Oceans*, *120*, 2370–2384. https://doi.org/10.1002/2014JC010516

Friedland, K. D., & Hare, J. A. (2007). Long-term trends and regime shifts in sea surface temperature on the continental shelf of the northeast United States. *Continental Shelf Research*, *27*(18), 2313–2328. https://doi.org/10.1016/j.csr.2007.06.001

Fulweiler, R. W., Oczkowski, A. J., Miller, K. M., Oviatt, C. A., & Pilson, M. E. Q. (2015). Whole truths vs. half truths–And a search for clarity in long-term water temperature records. *Estuarine, Coastal and Shelf Science*, *157*, A1–A6. https://doi.org/10.1016/j.ecss.2015.01.021

Gawarkiewicz, G., Chen, K., Lynch, J. F., Grothues, T. M., Newhall, A., & Lin, Y. T. (2014). Impacts of the warming of the Continental Shelf in spring 2012 on acoustic propagation conditions and fish distributions north of Cape Hatteras. *The Journal of the Acoustical Society of America*, *135*(4), 2154–2154. https://doi.org/10.1121/1.4876982

Gawarkiewicz, G., Todd, R. E., Plueddemann, A. J., Andres, M., & Manning, J. P. (2012). Direct interaction between the Gulf Stream and the shelfbreak south of New England. *Scientific Reports*, *2*(1), 553. https://doi.org/10.1038/srep00553

Gawarkiewicz, G., Todd, R. E., Zhang, W., Partida, J., Gangopadhyay, A., Monim, M. U. H., et al. (2018). The changing nature of shelf-break exchange revealed by the OOI Pioneer Array. *Oceanography*, *31*(1), 60–70. https://doi.org/10.5670/oceanog.2018.110

Han, G., & Niedrauer, T. (1981). Hydrographic observations and mixing processes in the New York Bight, 1975–1977. *Limnology and Oceanography*, *26*(6), 1126–1141. https://doi.org/10.4319/lo.1981.26.6.1126

Hopkins, T. S., & Garfield, N. III (1979). Gulf of Maine intermediate water. *Journal of Marine Research*, *37*(1), 103–109.

Houghton, R. W., Schlitz, R., Beardsley, R. C., Butman, B., & Chamberlin, J. L. (1982). The Middle Atlantic Bight cold pool: Evolution of the temperature structure during summer 1979. *Journal of Physical Oceanography*, *12*(10), 1019–1029. https://doi.org/10.1175/1520-0485(1982)012<1019:TMABCP>2.0.CO;2

Hurrell, J. W., Deser, C. (2010). North Atlantic climate variability: The role of the North Atlantic Oscillation. *Journal of Marine Systems*, *79*(3–4), 231–244. https://doi.org/10.1016/j.jmarsys.2009.11.002

Joyce, T. M., Kwon, Y. O., Seo, H., & Ummenhofer, C. C. (2019). Meridional Gulf Stream shifts can influence wintertime variability in the North Atlantic storm track and Greenland blocking. *Geophysical Research Letters*, *46*, 1702–1708. https://doi.org/10.1029/2018GL081087

Kang, D., & Curchitser, E. N. (2013). Gulf Stream eddy characteristics in a high-resolution ocean model. *Journal of Geophysical Research: Oceans*, *118*, 4474–4487. https://doi.org/10.1002/jgrc.20318

Kang, D., & Curchitser, E. N. (2015). Energetics of eddy–mean flow interactions in the Gulf Stream region. *Journal of Physical Oceanography*, *45*(4), 1103–1120. https://doi.org/10.1175/JPO-D-14-0200.1

Kavanaugh, M. T., Rheuban, J. E., Luis, K. M., & Doney, S. C. (2017). Thirty-three years of ocean benthic warming along the US northeast continental shelf and slope: Patterns, drivers, and ecological consequences. *Journal of Geophysical Research: Oceans*, *122*, 9399–9414. https://doi.org/10.1002/2017JC012953

Kerr, R. A. (2000). A North Atlantic climate pacemaker for the centuries. *Science*, *288*(5473), 1984–1985. https://doi.org/10.1126/science.288.5473.1984

Ketchum, B. H., & Corwin, N. (1964). The persistence of 'winter' water on the continental shelf south of Long Island, New York. *Limnology and Oceanography*, *9*(4), 467–475. https://doi.org/10.4319/lo.1964.9.4.0467

Lentz, S. J. (2017). Seasonal warming of the Middle Atlantic Bight Cold Pool. *Journal of Geophysical Research: Oceans*, *122*, 941–954. https://doi.org/10.1002/2016JC012201

Miller, T. J., Hare, J. A., & Alade, L. A. (2016). A state-space approach to incorporating environmental effects on recruitment in an age-structured assessment model with an application to southern New England yellowtail flounder. *Canadian Journal of Fisheries and Aquatic Sciences*, *73*(8), 1261–1270. https://doi.org/10.1139/cjfas-2015-0339

Nye, J. A., Joyce, T. M., Kwon, Y. O., & Link, J. S. (2011). Silver hake tracks changes in Northwest Atlantic circulation. *Nature Communications*, *2*(1), 1–6.

Nye, J. A., Link, J. S., Hare, J. A., & Overholtz, W. J. (2009). Changing spatial distribution of fish stocks in relation to climate and population size on the Northeast United States continental shelf. *Marine Ecology Progress Series*, *393*, 111–129. https://doi.org/10.3354/meps08220

Ou, H. W., & Houghton, R. (1982). A model of the summer progression of the cold-pool temperature in the Middle Atlantic Bight. *Journal of Physical Oceanography*, *12*(10), 1030–1036. https://doi.org/10.1175/1520-0485(1982)012<1030:AMOTSP>2.0.CO;2

Richaud, B., Kwon, Y. O., Joyce, T. M., Fratantoni, P. S., & Lentz, S. J. (2016). Surface and bottom temperature and salinity climatology along the continental shelf off the Canadian and US East Coasts. *Continental Shelf Research*, *124*, 165–181. https://doi.org/10.1016/j.csr.2016.06.005

Shchepetkin, A. F., & McWilliams, J. C. (2005). The regional oceanic modeling system (ROMS): A split-explicit, free-surface, topography-following-coordinate oceanic model. *Ocean Modelling*, *9*(4), 347–404. https://doi.org/10.1016/j.ocemod.2004.08.002

Shearman, R. K., & Lentz, S. J. (2010). Long-term sea surface temperature variability along the US East Coast. *Journal of Physical Oceanography*, *40*(5), 1004–1017. https://doi.org/10.1175/2009JPO4300.1

Sullivan, M. C., Cowen, R. K., & Steves, B. P. (2005). Evidence for atmosphere–ocean forcing of yellowtail flounder (*Limanda ferruginea*) recruitment in the Middle Atlantic Bight. *Fisheries Oceanography*, *14*(5), 386–399. https://doi.org/10.1111/j.1365-2419.2005.00343.x

Zhang, W. G., & Gawarkiewicz, G. G. (2015). Dynamics of the direct intrusion of Gulf Stream ring water onto the Mid-Atlantic Bight shelf. *Geophysical Research Letters*, *42*, 7687–7695. https://doi.org/10.1002/2015GL065530